

# Image Sensor Modeling: Color Measurement at Low Light Levels

Mehdi Rezagholizadeh and James J. Clark

Centre for Intelligent Machines, McGill University, 3480 University Street, Montreal, Quebec, Canada, H3A 0E9  
E-mail: mehdi.rezagholizadeh@mail.mcgill.ca

**Abstract.** The investigation of low light imaging is of high importance in the field of color science from different perspectives. One of the most important challenges that arises at low light levels is the issue of noise or, more generally speaking, low signal-to-noise ratio (SNR). In the present work, effects of different image sensor noises, such as photon noise, dark current noise, read noise, and quantization error are investigated in low light color measurements. In this regard, a typical image sensor is modeled and employed for this study. A detailed model of noise is considered in the process of implementing the image sensor model to guarantee the precision of the results. Several experiments have been performed over the implemented framework and the results show the following: first, photon noise, read noise, and quantization error lead to uncertain measurements distributed around the noise free measurements and these noisy samples form an elliptical shape in the chromaticity diagram; second, even for an ideal image sensor, in very dark situations, stable measurement of color is impossible due to the physical limitation imposed by the fluctuations in photon emission rate; third, dark current noise reveals dynamic effects on color measurements by shifting their chromaticities towards the chromaticity of the camera black point; fourth, dark current dominates the other sensor noise types in the image sensor in terms of affecting measurements. Moreover, an SNR sensitivity analysis against the noise parameters is presented over different light intensities. © 2014 Society for Imaging Science and Technology.

[DOI: 10.2352/J.ImagingSci.Technol.2014.58.3.030401]

## INTRODUCTION

The human visual system is able to work under various lighting conditions. It is desirable to have imaging devices, such as cameras, that are able to operate in similar light levels. The ability of the human visual system to work even under low light situations leads to the importance of studying low light levels. However, most of the theories, measures, models, and methods in color science are developed for high intensities.<sup>1</sup> These theories, measures, methods, and models cannot be used for low light situations, since they fail to comply with the necessary conditions for which they are feasible. For instance, a color difference formula that is derived for photopic conditions (i.e., luminance levels greater than 5 cd/m<sup>2</sup>) cannot be leveraged in evaluating techniques developed for assessing dark images.<sup>2</sup> This issue implies the importance of investigating low light conditions. Moreover, addressing low light or, more generally speaking, low signal-to-noise level situations has a wide range of

applications in photography,<sup>3</sup> designing biosensors,<sup>4</sup> image processing,<sup>5</sup> machine vision, and color science.<sup>6</sup>

For both imaging devices and the human visual system, as the light level goes down, the effect of noise becomes more significant.<sup>6</sup> In this situation, an imaging device will acquire a noisy signal with a low value of signal-to-noise ratio (SNR). In human vision, lower signal-to-noise level results in changes in the appearance of measured colors. Several works have discussed the impact of light level on human color perception.<sup>7–10</sup> It is unanimously accepted that reducing the light level gives rise to color shifts, and this effect is mostly attributed to the rod intrusion into the mesopic vision (dim light situation in which both rods and cones contribute to vision).<sup>11,12</sup> However, the issue of noise at low light levels is still an open problem for artificial image sensors.

To the best of our knowledge, the effect of noise at low light levels on the color measurements of imaging devices has not been addressed yet. One of the most recent works concerning this topic is the work performed by Kirk and O'Brien, proposing a tone mapping approach to convert high dynamic low light images to a perceptually closer result to the human mesopic vision experience.<sup>13</sup> However, the authors did not take into account any noise type in their mesopic color appearance modeling and left it as a future work.

Our article is concerned with modeling the performance of color image sensors under low signal-to-noise ratios. Our methodology involves tracking photons in the imaging sensor pipeline from the emission to the detection and recording level. In this regard, physical rules governing photon emission are employed to estimate the low light version of quantities describing the light coming to the imaging device; then, an image sensor model is implemented and leveraged to study the luminance and noise induced effects on the sensor color measurements. Camera or image sensor models have been presented in different works.<sup>14,15</sup> The rationale behind modeling digital camera imaging systems is, first, to reconstruct hyperspectral images taken by spectrometers, or to be used in computer graphics applications<sup>16</sup>; second, to evaluate the camera design and output image quality, or to optimize the performance of the camera in terms of some adjustable parameters (e.g., exposure time or ISO setting).<sup>17,18</sup>

In terms of application, the results of this study can be utilized in developing low light image quality measures, introducing efficient denoising algorithms, developing realistic color noise perception models,<sup>19</sup> addressing low

Received May 4, 2014; accepted for publication Sept. 18, 2014; published online Oct. 7, 2014. Associate Editor: Marius Pedersen.

1062-3701/2014/58(3)/030401/11/\$25.00

signal-to-noise levels in digital cameras, and developing an automatic labeling system for micro-array sensor biochips.<sup>20</sup>

The remainder of this article is organized as follows. The background for light emission is presented in the second section followed by introduction of the image sensor modeling in the third section. Experiments, results, and discussion are reported in the fourth section. Finally, the fifth section concludes the article.

## BACKGROUND

Light consists of energy packets called *photons*. Photons are characterized by their frequency and polarization state.<sup>21</sup> Each photon carries an amount of energy determined by its frequency. This energy is equal to  $\{hc/\lambda\}$ , where  $h = 6.626,176 \times 10^{-34}$  (J s) is the Planck constant,  $c = 2.997,925 \times 10^8$  (m/s) represents the light speed, and  $\lambda$  denotes the wavelength (inverse of frequency) of the photon. Photon emission from a light source follows a Poisson distribution. For a monochromatic light source of a particular wavelength  $\lambda_0$  and known average number of emitted photons per second  $g$ , the probability of emitting  $n$  photons per unit of time can be obtained as follows<sup>22</sup>:

$$P(g, n) = \frac{g^n e^{-g}}{n!}. \quad (1)$$

Given the spectral radiance,  $L(\lambda)$ , the average emitted number of photons, per unit time, per unit area, per unit steradian, for a central wavelength  $\lambda_0$  can be obtained by calculating the following integral over an infinitely small range of  $[\lambda_0 - \delta/2, \lambda_0 + \delta/2]$ :

$$g(\lambda_0) = \frac{1}{hc} \int_{\lambda_0 - \delta/2}^{\lambda_0 + \delta/2} \lambda L(\lambda) d\lambda. \quad (2)$$

The wavelength range of the spectrum,  $[\lambda_{\min}, \lambda_{\max}]$ , can be discretized into  $N$  intervals of the length  $\delta$  such that  $\{\lambda_{\max} - \lambda_{\min} = N\delta\}$ . Hence,  $g(\lambda_i)$  of the  $i$ th wavelength bin can be approximated as

$$g(\lambda_i) = \frac{1}{hc} \int_{\lambda_i - \delta/2}^{\lambda_i + \delta/2} \lambda L(\lambda) d\lambda \approx \frac{\lambda_i L(\lambda_i) \delta}{hc}. \quad (3)$$

Let  $L(\lambda)$  represent the high intensity radiance of a light. Our goal is to derive an estimation of this spectral radiance at an arbitrary lower intensity. The high intensity spectral radiance is the most complete description of the light and this quantity at any lower intensity can be predicted from the given high intensity spectrum as described in the following.

The Poisson distribution,  $\text{Pois}(g(\lambda_i))$ , corresponding to each bin of the high intensity spectral radiance is fully characterized by knowing the  $g(\lambda_i)$  values. We define the intensity factor  $F \leq 1$ , which is a multiplier to change the light level. The estimated spectral radiance after applying the intensity factor  $F$  can be obtained by drawing samples,  $\{\tilde{G}_F(\lambda_i)\}_1^N$ , from  $\{\text{Pois}(F \times g(\lambda_i))\}_1^N$  distributions. Hence, the estimated spectral radiance,  $\tilde{L}_F(\lambda)$ , for the intensity factor

$F$  and central wavelength  $\lambda_i$  is given by

$$\tilde{L}_F(\lambda_i) = \frac{\tilde{G}_F(\lambda_i) \times hc}{\lambda_i \delta}. \quad (4)$$

By taking this approach, we can establish the effect of shot noise on estimates of low light spectral radiances. It is worth mentioning that  $\tilde{L}_{FN}(\alpha, \beta, \lambda)$ , which denotes the quantal number of photons falling on the location  $(\alpha, \beta)$  of the image sensor in photons/sec/m<sup>2</sup>/sr/nm, can be obtained from the radiance quantity,  $\tilde{L}_F(\alpha, \beta, \lambda)$ , as

$$\tilde{L}_{FN}(\alpha, \beta, \lambda) = \frac{\tilde{L}_F(\alpha, \beta, \lambda) \times \lambda}{hc}. \quad (5)$$

## IMAGE SENSOR MODELING

A typical digital camera is comprised of the following elements: an optical system, an image sensor, and an image processor.<sup>16</sup> The focus of this section is on modeling and simulating the image sensor of a digital camera. We consider the image formation model, noise model, and analog-to-digital converter (ADC) components in the image sensor model. Figure 1 shows a diagram of the image sensor model, which is a modified version of the model introduced in Ref. 18.

When the shutter of a camera opens, a stream of photons enters the camera and falls on the image sensor. A color image sensor consists of three sensor types, which usually are referred to as R, G, and B sensors. The exposure setting determines the number of photons captured by the sensors. Each sensor type has a specific spectral quantum efficiency (i.e., the proportion of electrons generated as a result of photon catches for an area of 1 (m<sup>2</sup>) that subtends 1 (sr)). A pixel of an image sensor consists of a photodetector, a color filter, and a readout circuit. The rain of photons hitting the photodetector produces a photocurrent. This photocurrent together with the photodetector dark current, which will be explained later, is accumulated during the integration time as far as the sensor capacity allows. The maximum sensor charge capacity is known as full-well capacity and determines the level of saturation for each sensor. When the integration time is over, the readout circuit is responsible for measuring the voltage produced in the pixels. This process is prone to noise, known as the readout noise. The structure of the readout circuit is the main difference between CCD and CMOS type image sensors.

### Noise Model

Noise can be defined as any unwanted event that hampers the image quality. In our simulation framework, we assume an additive model for the noise and the following noise types are considered as the most significant sources of noise underlying the image distortion.

#### Photon Shot Noise

Photon shot noise can be defined as the variation in the number of photons emitted from the light source and,

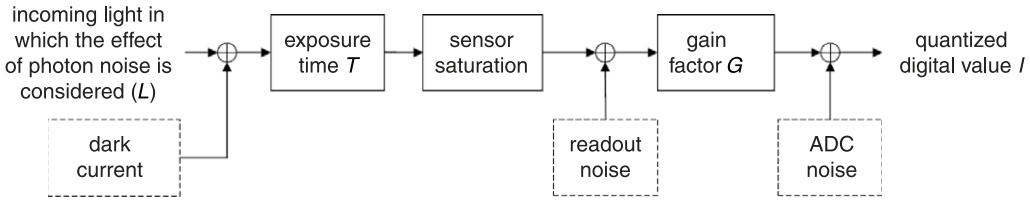


Figure 1. Image sensor prototype for a single channel.

consequently, the number of photons detected in the image sensor at different times. This phenomenon is rooted in the probabilistic nature of photon emission, as explained in the background above.

#### Dark Current Noise

The current produced inside the image sensor in the absence of light is referred to as the *dark current noise*. This current is not generated as a result of photogeneration but as a result of the impurities existing in the silicon wafer.<sup>23</sup> Dark current noise is also known as thermal noise and ambient temperature has a large influence on its amplitude. Dark current introduces shot noise to the measurement<sup>23</sup> and can be modeled by a Poisson distribution with a variance of  $(\sigma_{\text{dark}}^{\kappa})^2$  for the  $\kappa$  sensor type. Since the variance of a Poisson distribution is equal to its expected value, the parameter  $(\sigma_{\text{dark}}^{\kappa})^2$  represents the average number of generated electrons as a result of dark current for each pixel per unit time.

$$N_{\text{dark}}^{\kappa}(\alpha, \beta) \sim \text{Pois}((\sigma_{\text{dark}}^{\kappa})^2). \quad (6)$$

#### Read Noise

Read noise refers to the noise in the readout circuit, caused by an on-chip amplifier, and can be modeled as a white Gaussian distribution with standard deviation  $\sigma_{\text{read}}$ .<sup>14</sup> Readout noise limits the dynamic range of image sensors.

$$N_{\text{read}} \sim N(0, \sigma_{\text{read}}). \quad (7)$$

#### Quantization Noise

In the last step of generating the digital image in the image sensor prototype, the amplified voltage should be quantized into digital values. Quantization error introduced in this step is known as quantization noise and represented as  $\sigma_{\text{adc}}$ . The noise induced by the amplifier of the analog-to-digital conversion unit (ADC) is considered negligible.

#### Pixel Measurement Model

The voltage produced by an image sensor can be obtained by the following formula:

$$V^{\kappa}(\alpha, \beta) = G_{\text{Ve}^-} \times f_{\text{sat}} \left( T \times \int_{\lambda_{\min}}^{\lambda_{\max}} \tilde{L}_{FN}(\alpha, \beta, \lambda) Q_e^{\kappa}(\lambda) d\lambda + T \times N_{\text{dark}}^{\kappa}(\alpha, \beta) \right), \quad (8)$$

where  $\kappa \in \{\text{R}, \text{G}, \text{B}\}$ ,  $T$  indicates the exposure time in s,  $G_{\text{Ve}^-}$  is the conversion gain in V/e<sup>-</sup>,  $\tilde{L}_{FN}(\alpha, \beta, \lambda)$  represents the number of incident photons at the location  $(\alpha, \beta)$  of the image sensor obtained from the spectral radiance  $\tilde{L}_F$  at intensity factor  $F$  in photons/s/m<sup>2</sup>/sr/nm,  $Q_e^{\kappa}(\lambda)$  is the quantum efficiency of the  $\kappa$  sensor, in e<sup>-</sup> m<sup>2</sup> sr/photons,  $N_{\text{dark}}^{\kappa}(\alpha, \beta)$  represents the number of electrons generated as a result of dark noise in the  $\kappa$  channel for the pixel  $(\alpha, \beta)$ , and  $f_{\text{sat}}(\cdot)$  indicates the saturation function of the sensor.

The quantum efficiency curve for the  $\kappa$  sensor type is defined as the proportion of the number of electrons generated by the sensor,  $N_e^{\kappa}$ , to the number of incident photons with the wavelength  $\lambda$ ,  $N_{\text{ph}}^{\kappa}$ .<sup>24</sup>

$$Q_e^{\kappa}(\lambda) = \frac{N_e}{N_{\text{ph}}^{\kappa}(\lambda)}. \quad (9)$$

The voltage measured by the readout circuit is given by

$$\tilde{V}^{\kappa}(\alpha, \beta) = V^{\kappa}(\alpha, \beta) + N_{\text{read}}(\alpha, \beta). \quad (10)$$

The raw output image of the camera can be obtained after applying the gain factor and then the quantization process as follows:

$$I^{\kappa}(\alpha, \beta) = [G \times \tilde{V}^{\kappa}(\alpha, \beta)]_{n_b}. \quad (11)$$

In the above equation,  $[.]_{n_b}$  represents the “ $n_b$ -bit” quantization operation that outputs the integer part of the given operand,  $G \times \tilde{V}^{\kappa}(\alpha, \beta)$ , in the range of  $[0, 2^{n_b} - 1]$ . Hence, the quantization noise of the  $\kappa$ th channel at the location  $(\alpha, \beta)$  of the image is given by

$$\sigma_{\text{ADC}}(\alpha, \beta)^{\kappa} = I^{\kappa}(\alpha, \beta) - G \times \tilde{V}^{\kappa}(\alpha, \beta). \quad (12)$$

Finally, the signal-to-noise ratio can be defined as the ratio of the nonsaturated output of the noise free signal to the variance of the noise. The total variance of noise for each sensor type at each pixel location can be estimated as follows<sup>25</sup>:

$$\text{Var}^{\kappa}(\alpha, \beta) = V^{\kappa}(\alpha, \beta) \times G^2 + \sigma_{\text{read}}^2 \times G^2 + (\sigma_{\text{ADC}}^{\kappa}(\alpha, \beta))^2. \quad (13)$$

For nonsaturated pixels in the image, the SNR value of each channel can be obtained by the following formula<sup>18</sup>:

$$\begin{aligned} \text{SNR}^{\kappa}(\alpha, \beta) &= \\ &= \frac{\left[ G \times G_{\text{Ve}^-} \times T \times \int_{\lambda_{\min}}^{\lambda_{\max}} \tilde{L}_{FN}(\alpha, \beta, \lambda) Q_e^{\kappa}(\lambda) d\lambda \right]_{n_b}^2}{V^{\kappa}(\alpha, \beta) \times G^2 + \sigma_{\text{read}}^2 \times G^2 + \sigma_{\text{ADC}}^2}. \end{aligned} \quad (14)$$

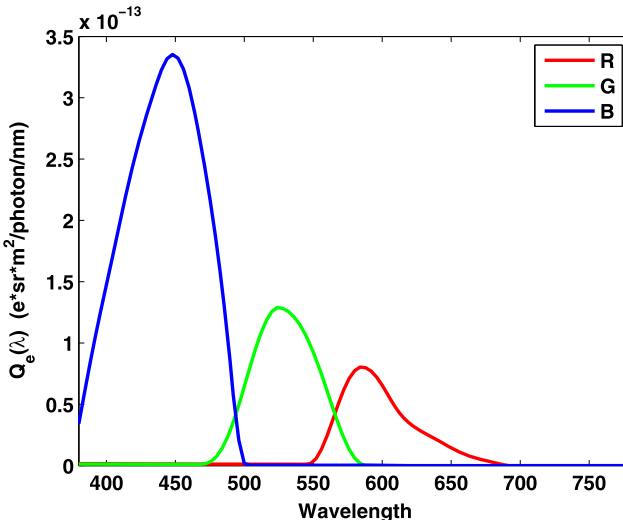


Figure 2. The quantum efficiency curves of image sensors in  $e^- \text{ sr m}^2/\text{photon}/\text{nm}$ .

## EXPERIMENTS, RESULTS AND DISCUSSION

We designed a set of experiments intended to investigate the effects of different noise types on the color measurements of image sensors. The experiments were performed using the spectral radiances selected from “A Data Set for Color Research,” prepared by Barnard et al.<sup>26</sup> The dataset contains the spectral sensor sensitivity curves of the Sony DXC-930 three-chip CCD video camera and the spectra of 23 of the Macbeth color patches illuminated by 26 different light sources. The Sony DXC-930 sensor sensitivity curves are used in the image sensor simulation phase of this work and the spectra, which we refer to as the RGB598 spectral database, are leveraged for our experiments and evaluation of the simulation. The sensor quantum efficiency curves are shown in Figure 2. Each spectrum is sampled in 4 nm steps from 380 to 780. Details about this database can be found in Ref. 26. The chromaticities spanned by the 598 spectra of this database are shown in the chromaticity diagram in Figure 3, and, among these points, 20 points are selected for the sake of our experiments. First, each spectral radiance is scaled to have a spectrum with a luminance value of 100 ( $\text{cd/m}^2$ ); then, to obtain a lower luminance value, the spectrum is used as  $L(\lambda)$  in Eqs. (3)–(5) to estimate the corresponding low intensity spectral radiance  $\tilde{L}_F$  at the intensity factor  $F$ . It is worth mentioning that since the luminance of the scaled spectral radiances are set to 100 at the intensity factor  $F = 1$ , the approximate luminance value of  $\tilde{L}_F$  can be obtained as  $F \times 100$ .

For each data point, the raw output of the image sensor is generated from the modeled framework at a specific condition defined for each experiment. The parameters selected for the image sensor model at a temperature of 20°C are listed in Table I. The camera black RGB for Sony DXC-930 is provided in the RGB598 database and this value is scaled to obtain the variance of dark noise  $(\sigma_{\text{dark}}^\kappa)^2$ . Full-well capacity, read noise standard deviation  $(\sigma_{\text{read}})$ , and the conversion gain ( $G_{\text{Ve}^-}$ ) are selected from Ref. 16. Based on these selected

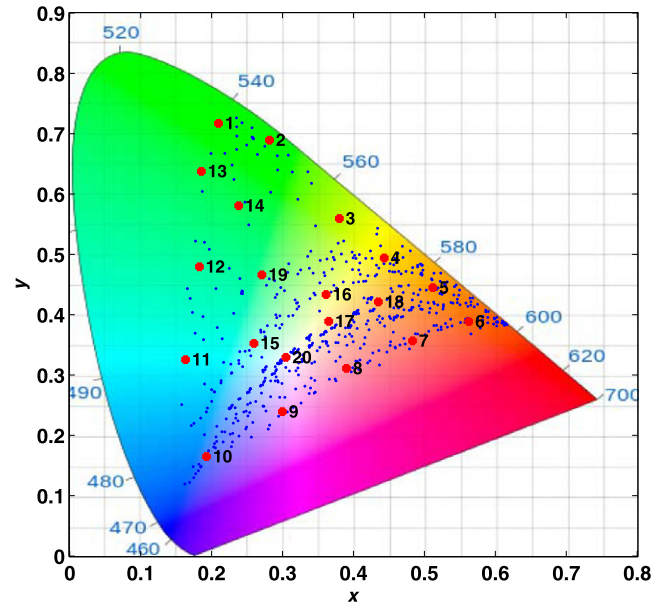


Figure 3. The chromaticity values spanned by the RGB598 spectral database are indicated by blue dots. The selected data points for the experiment are marked as red asterisks with designated numeric indices.

**Table I.** Parameters of the model at 20°C.

| Sensor parameter                                                  | Parameter value |
|-------------------------------------------------------------------|-----------------|
| $G_{\text{Ve}^-}$ ( $\text{V/e}^-$ )                              | 0.0002          |
| $(\sigma_{\text{dark}}^\kappa)^2$ ( $\text{e}^-/\text{pixel/s}$ ) | [195, 230, 218] |
| $\sigma_{\text{read}}$ ( $\text{e}^-$ )                           | 4               |
| $G$                                                               | 141.67          |
| Full-well capacity ( $\text{e}^-$ )                               | 9000            |
| $T$ (s)                                                           | 1               |
| $n_b$                                                             | 8               |

values, the parameter  $G$  is determined such that the output of the sensor best fits the empirical measurements given in the RGB598 database.

To account for uncertainties imposed by noise, 200 measurements are recorded for each sample in each trial. The measured samples ( $I$ ) are converted to the  $XYZ$  space ( $I_{XYZ}$ ), and then to the  $xy$ -chromaticity space. This transformation is given by

$$I_{XYZ} = M \times I, \\ M = (T_{XYZ} \times T_{XYZ}^t) \times (C \times T_{XYZ}^t)^{-1}, \quad (15)$$

where  $T_{XYZ}$  and  $C$  are  $(3 \times N)$  matrices representing the  $XYZ$  color matching function and the camera sensitivity curves respectively. The camera sensitivity curves can be obtained from the quantum efficiency function,  $Q_e^\kappa(\lambda_i)$ , as follows:

$$C^\kappa(\lambda) = G_{\text{Ve}^-} \times G \times Q^\kappa(\lambda), \\ Q^\kappa(\lambda_i) = \frac{hc}{\lambda_i} \times Q_e^\kappa(\lambda_i) \quad \kappa \in \{\text{R, G, B}\}, \quad i \in \{1, 2, \dots, N\}. \quad (16)$$

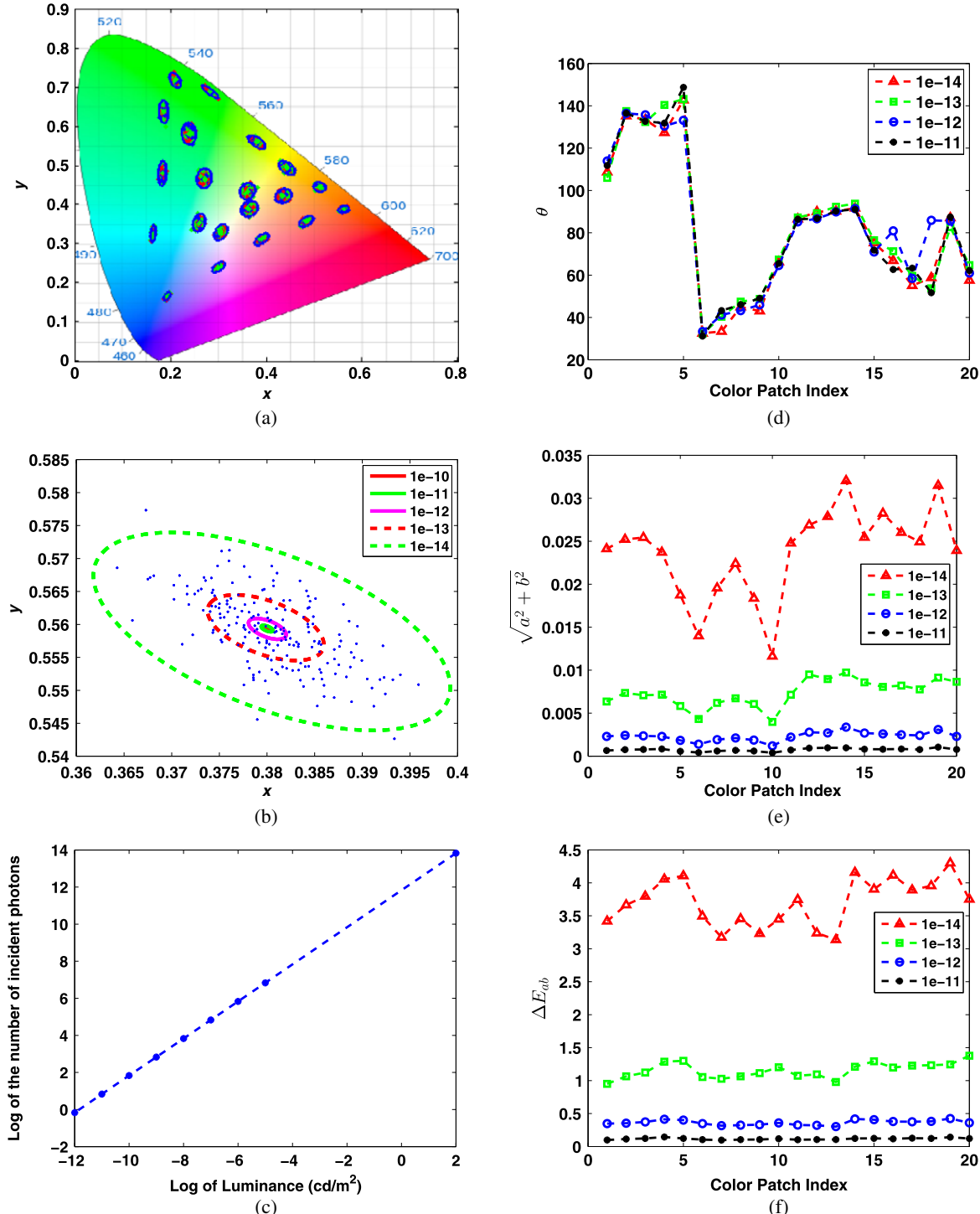


**Figure 4.** The results of scenario I performed over the RGB598 database. (a) The generated samples for each selected data point of the RGB598 database together with the fitted ellipses to those samples are plotted. (b) The generated samples and the fitted ellipses for different intensity factors for data point number 3. (c) The log number of incident photons at different luminance levels for color patch number 3 is depicted. (d) The estimated inclination angles of ellipses obtained from the PCA algorithm for different intensity factors are shown for all color patches. (e) The sizes of fitted ellipses corresponding to different intensity factors for all selected color patches are compared. (f) The average of  $\Delta E_{ab}$  values over the samples of each intensity factor.

Here a question may arise, which is “is it correct to use CIE photopic colorimetry in a low light mesopic range?” There are two reasons behind the choice of CIE XYZ color matching functions: first, CIE photopic colorimetry is commonly used in cameras in the process of creating the

output image; second, to the best of our knowledge, current camera technology does not use any known color space or model specific for mesopic conditions. A CIE system for mesopic photometry was proposed in Ref. 27; however, the use of it is still not widespread.

The experiments were carried out over three scenarios and followed by an SNR sensitivity analysis. Before explaining the results, we state the main assumptions and considerations of this work as follows.

- (1) The temperature is assumed constant, hence the dark noise parameters are fixed during the experiments.
- (2) The noise model is additive in the image sensor simulation framework.
- (3) The image sensor linearly responds to light intensity variations before its saturation limit. Sensor linearity is discussed in Ref. 28 more profoundly. In Ref. 28, Barnard and Funt mention that “The Sony DXC-930 camera that we used for our experiments is quite linear for most of its range, provided it is used with gamma disabled.”
- (4) Raw output images are considered for our analysis.
- (5) Reset noise, photodetector response nonuniformity (PRNU), and dark signal nonuniformity (DSNU) are not incorporated in our modeling, and, for our research, we assume that their impact on the introduced model is negligible. For further details the reader can refer to Ref. 25.

#### **Scenario I: Ideal Image Sensor and Light Intensity**

In the first scenario, we consider the case where there is no noise corrupting the output image, we have a perfect image sensor able to detect single photon events, and the sensor can respond without saturation. We want to investigate at which luminance value the photon noise becomes significant. In this regard, twenty data points shown in Fig. 3 are considered for this experiment. The log of the intensity factor is set to values  $\log(F) \in \{0, -7, -8, -9, -10, -11, -12, -13, -14\}$ . The results of the experiment are shown in Figure 4. Fig. 4(a) indicates that the generated samples form an elliptic shape in the chromaticity diagram. The principal component analysis (PCA) algorithm is used to find a fitted ellipse for the generated samples of each data point.<sup>29</sup>

The generated samples and the fitted ellipses of the third data point for different intensity factors, and the number of incident photons on the image sensor for various luminance values are plotted in Figs. 4(b) and 4(c) respectively. In Fig. 4(b), the distance between consecutive ellipses grows exponentially as the light intensity decreases. Figs. 4(d) and 4(e) show the inclination angle and size of the fitted ellipses for some intensity factors. The size of each ellipse is approximated as  $\sqrt{a^2 + b^2}$ , where  $a$  and  $b$  represent the sizes of the semi-major and semi-minor axes of the ellipse. The inclination angle represents the angle between the semi-major axis and the  $x$ -axis of the  $xy$ -chromaticity space. The results indicate that the inclination angles, with a good approximation, are independent of the intensity level; however, the size of the ellipses inversely changes with intensity, proving that even if we had an ideal image sensor with no internal noise, we still had to deal with the photon noise and uncertainties imposed by physical limitations. It should be borne in mind that the photon noise becomes

noticeable at very low light levels, when the number of incident photons is less than 100. Since distances in the chromaticity diagram do not correspond to the human visual system color discriminability,  $\Delta E_{ab}$  is used as a figure of merit to show to what extent the effect of noise on color measurement at different intensities would be noticeable to a human observer from trial to trial. In this regard, for each data point, the  $\Delta E_{ab}$  measure is derived as follows:

- (1) the standard D65 illuminant is assumed as a white reference for the calculations at the luminance of  $100 \text{ cd/m}^2$  (the  $Y$  value of the reference white is kept constant during the entire experiment);
- (2) the  $XYZ$  values of each sample are scaled to equalize the  $Y$  value of the sample and that of the standard illuminant to be able to compare the color coordinates of the low intensity samples ( $F < 1$ ) and the high intensity sample generated at ( $F = 1$ );
- (3) CIELab coordinates of each sample are obtained;
- (4)  $\Delta E_{ab}$  is calculated between each sample and the average color coordinates of corresponding high intensity samples;
- (5) the average of  $\Delta E_{ab}$  values over the samples of each intensity factor is reported.

The result of  $\Delta E_{ab}$  calculation is shown in Fig. 4(f), indicating that as the light level falls off, the color change between different trials of each data point becomes more noticeable.

#### **Scenario II: Effects of Dark Current on Image Sensor Responses at Low Light Intensity**

It is shown in the first scenario that photon noise may bring about uncertainties in the measurements at very low light levels when the image sensor is deemed ideal and no other noises may disturb the measurement. In this subsection, the effect of dark current is examined separately from the other intrinsic noise types, when only photon noise and dark current are affecting the image sensor, and the sensor saturation function is not considered in the sensor model. The intensity factor is set to  $F \in \{1, 0.5, 0.1, 0.05, 0.01, 0.005, 0.001\}$  during each trial of the experiment. For the sake of this experiment, only the boundary data points (indices 1–13) from the initial 20 data points are picked to make the resulting figures clearer.

The results are shown in Figure 5, indicating that the dark noise may cause much more significant effects on the color measurement at lower intensities than the photon noise. The result is that the dark noise pushes the low intensity measurements towards the average chromaticity of the image sensor’s black point. In comparison to the photon noise, which became noticeable at intensity factors of the order of  $10^{-13}$  and lower, the dark current noise effect becomes visible for  $F \leq 0.1$ . This issue indicates the greater effects of dark noise compared with photon noise in hampering the quality of measurements. The angle of inclination of the ellipses,  $\theta$ , induced by the dark noise is

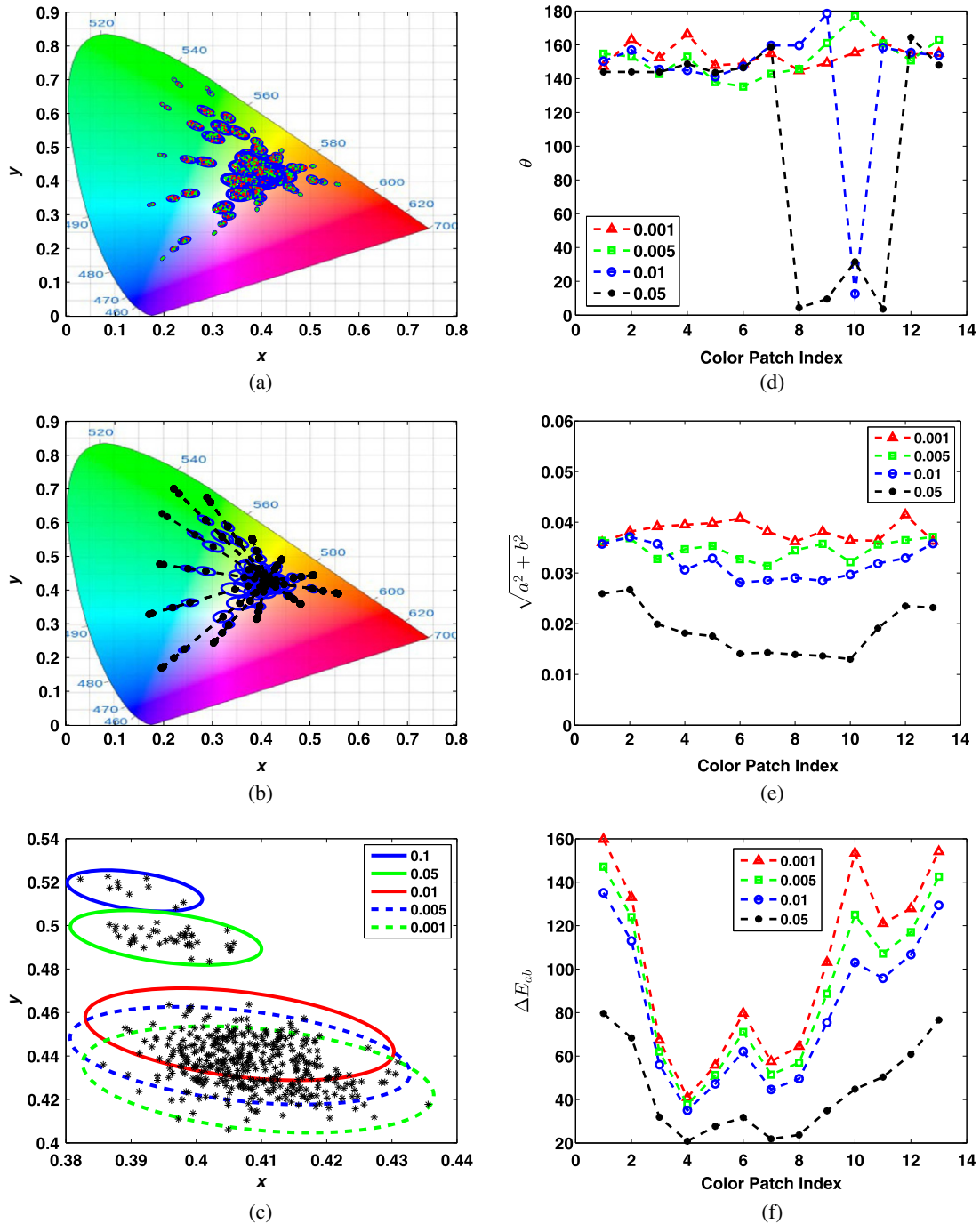


**Figure 5.** The results of scenario II performed over the RGB598 database when only photon noise and dark noise are taken into account in the image formation model. (a) Samples drawn for each selected data point of the RGB598 database and the ellipses fitted to the samples are plotted. (b) The subfigure in part (a) is regenerated after removing the samples and specifying the centers of the ellipses together with the line of movement of each data point with the light level. (c) The result of subfigure (a) is magnified for data point number 3. (d) The estimated inclination angles of ellipses obtained from the PCA algorithm for different intensity factors are shown for all color patches. (e) The sizes of fitted ellipses corresponding to different intensity factors for all selected color patches are compared. (f) The average of  $\Delta E_{ab}$  values over the samples of each intensity factor.

totally different from that of the photon noise. The ellipses are aligned more horizontally for low intensities, and their angles of inclination are more separated from each other in different intensity factors than the results of scenario I. Another interesting point is the opposite behavior of the ellipse size variations as a function of the color patch index

in different light intensities. In scenario I, the size of the ellipses is more uniform for lower intensity factors than for higher values of  $F$ ; however, in scenario II, the opposite of this pattern is exhibited, as seen in Fig. 5(e), where the size of lower intensity ellipses is more uniform than high intensity values.

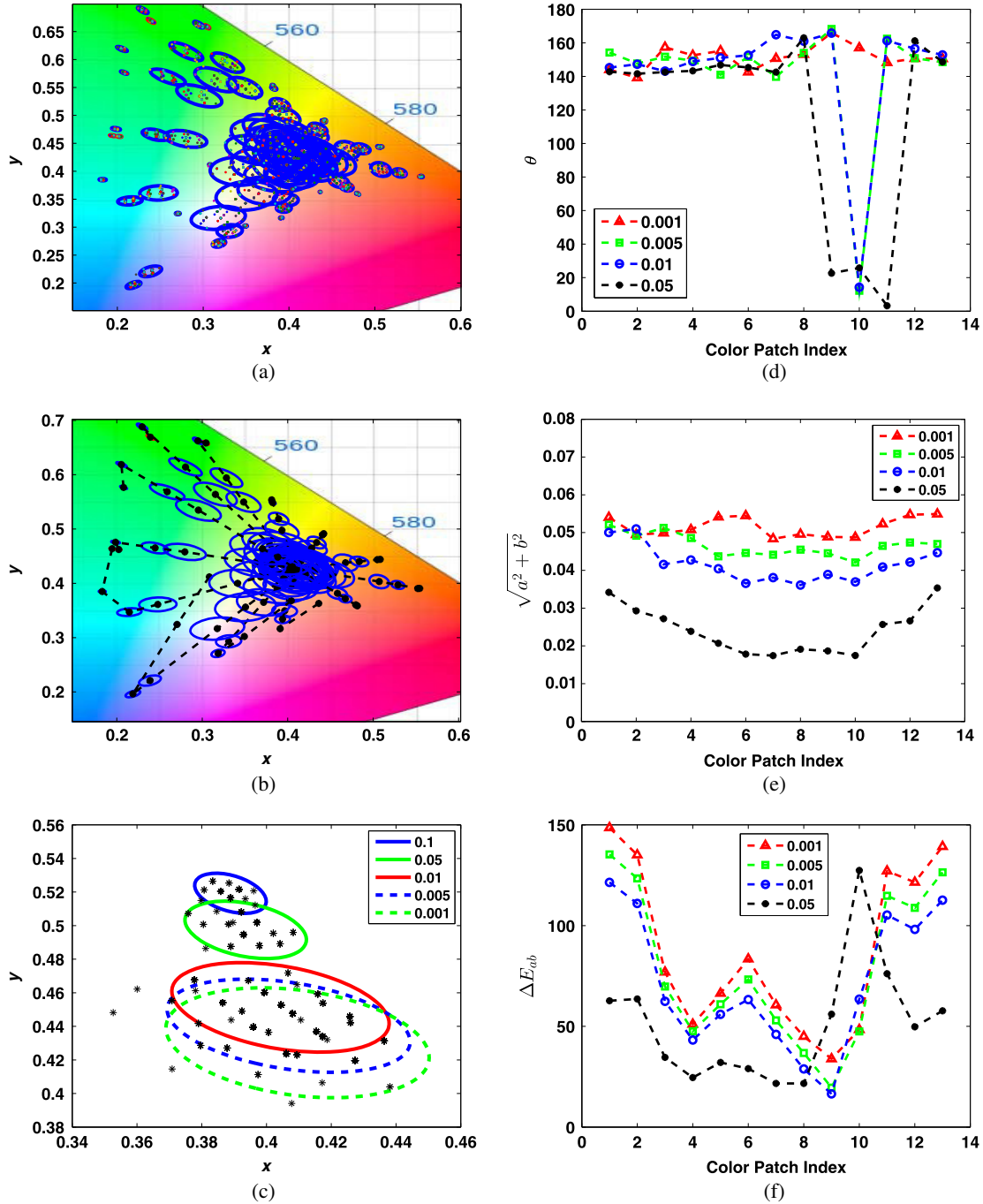


**Figure 6.** The results of scenario III performed over the RGB598 database when only photon noise and dark noise are taken into account in the image formation model. (a) Samples drawn for each selected data point of the RGB598 database and the ellipses fitted to the samples are plotted. (b) The subfigure in part (a) is regenerated after removing the samples and specifying the centers of the ellipses together with the line of movement of each data point with the light level. (c) The result of subfigure (a) is magnified for data point number 3. (d) The estimated inclination angles of ellipses obtained from the PCA algorithm for different intensity factors are shown for all color patches. (e) The sizes of fitted ellipses corresponding to different intensity factors for all selected color patches are compared. (f) The average of  $\Delta E_{ab}$  values over the samples of each intensity factor.

### Scenario III: Real Image Sensor Simulation

A similar scenario to scenario II is obtained with all noise types and the saturation function being active. In this experiment, only data points 1–13 are used. Figure 6 depicts the results. In Figs. 6(a) and 6(b), some data points make the sensor saturated at high intensity factors. Nonlinear effects imposed by these saturated samples are

explicitly revealed in Fig. 6(b). Moreover, the quantization level in the model leads to sparse samples in the chromaticity diagram, since it is not possible to have all chromaticity values in the output of the image sensor. Aside from this, the pattern of results of this scenario resembles that of scenario II, implying the dominant influence of dark noise in low light levels.

### SNR Sensitivity Analysis

In this subsection, an analysis of the sensitivity of the SNR value (given in Eq. (14)) to the parameters of dark current and read noise and including or excluding the quantization noise is presented. In this regard, only one noise is considered at a time (the other noises are deactivated in the model) and the parameters corresponding to that noise are set based on the values given in Table I. For the dark current and read noise, their corresponding parameters ( $(\sigma_{\text{dark}}^i)^2$  and  $\sigma_{\text{read}}$  respectively) are incremented by 10% and the change in the SNR value is averaged over 200 samples drawn in each trial. In Table I, the dark current parameter is given for the temperature of 20°C. Based on the dark current versus temperature curve given in Ref. 25 for a CCD image sensor, to increase the dark current by 10% at 20°C, the temperature should go up by approximately 1°C–2°C. The read noise parameter depends on the type of image sensor (CCD or CMOS) and the ISO setting of the camera. In Fig. 2 of Ref. 30, the read noise values of three image sensors are compared, and it is indicated that changing the ISO setting of a CCD chip between the consecutive steps may change the read noise standard deviation by around 10–20%.

The SNR change can be obtained by the following formula:

$$\Delta \text{SNR} (\%) = 100 \times \frac{\text{SNR}_1 - \text{SNR}_2}{\text{SNR}_1}, \quad (17)$$

where  $\text{SNR}_1$  and  $\text{SNR}_2$  represent the SNR values before and after incrementing the parameters respectively. Since the noise parameters used for  $\text{SNR}_2$  are greater than those of  $\text{SNR}_1$ , it is expected to have  $\text{SNR}_1 > \text{SNR}_2$ , and hence  $\Delta \text{SNR} > 0$ . A similar procedure is used to evaluate the quantization noise by comparing the SNR of the measurements with and without quantization noise. To avoid saturation effects on the results, the intensity factor is set to  $F \in \{0.1, 0.05, 0.01, 0.005, 0.001\}$ . This analysis is performed on the boundary color patches (indices 1–13), and the results for the data points {1, 3, 6, 8, 10, 12} together with the average result for all 13 points are reported for the R, G, and B sensor types in Figures 7–9. The maximum SNR change occurs in the smallest intensity factor for the dark current and read noise SNR sensitivity curves. However, this pattern is not seen in the quantization noise SNR sensitivity curves, as the R and G sensors have their maxima at different intermediate intensities. Figure 8 shows that the SNR change associated with read noise monotonically increases as the light level falls off. This statement is roughly true for the dark noise curves but it does not hold for the quantization noise sensitivity curves. In general, no consistent pattern can be found among the SNR sensitivity results for quantization noise, implying that this noise does not greatly depend on the intensity value. An interesting point that can be noted from Figs. 7 and 8 is that for each sensor type, the data points to which the sensor is more sensitive have lower SNR sensitivities in comparison with other data points. For example, in Figs. 7(a) and 8(a), the reddish color patch (index = 6)

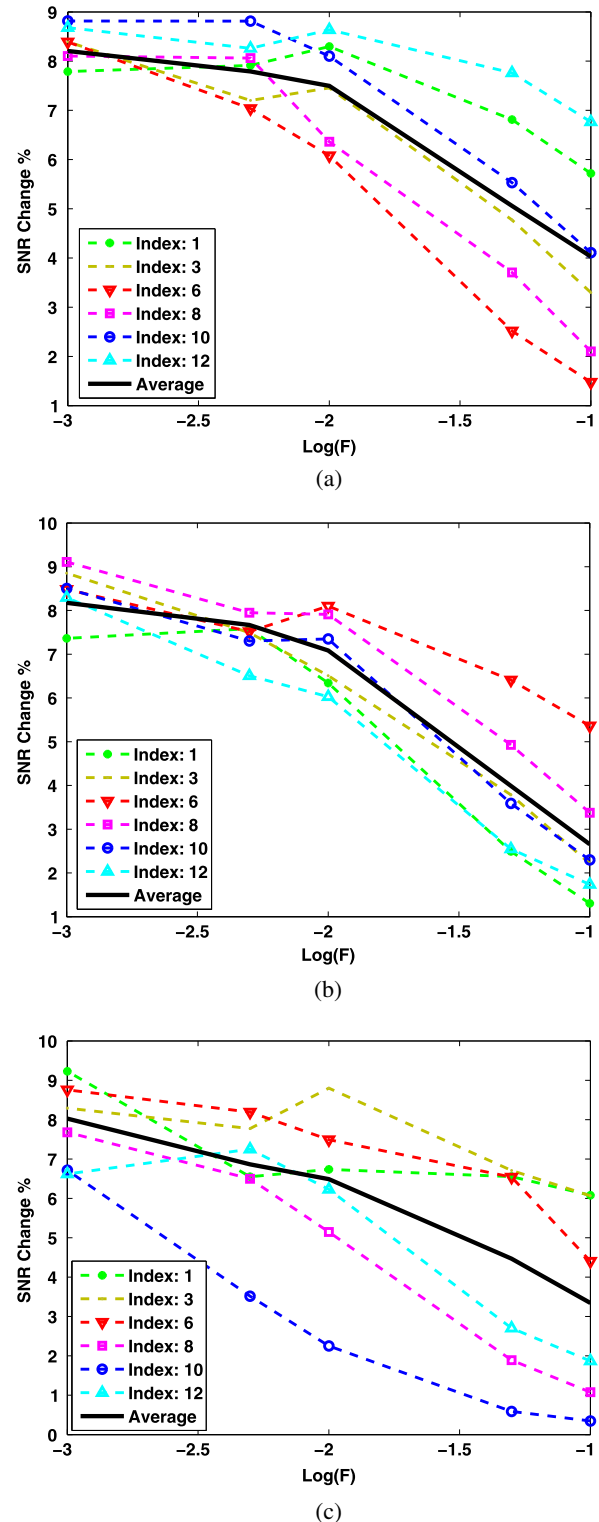
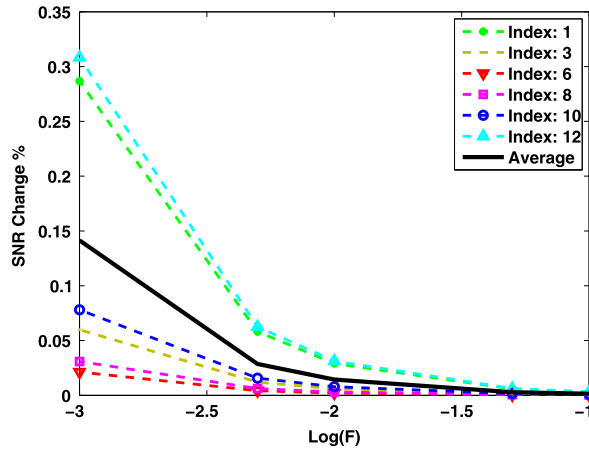
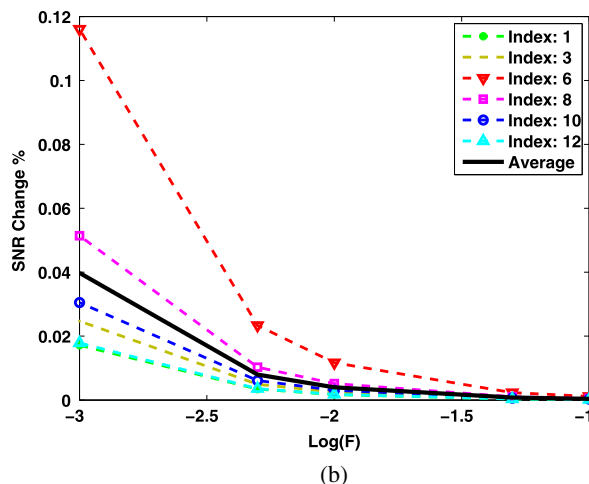


Figure 7. SNR sensitivity curves for the R, G, and B sensor types with respect to the dark current noise parameters for different color patches are plotted in (a), (b), and (c) respectively.

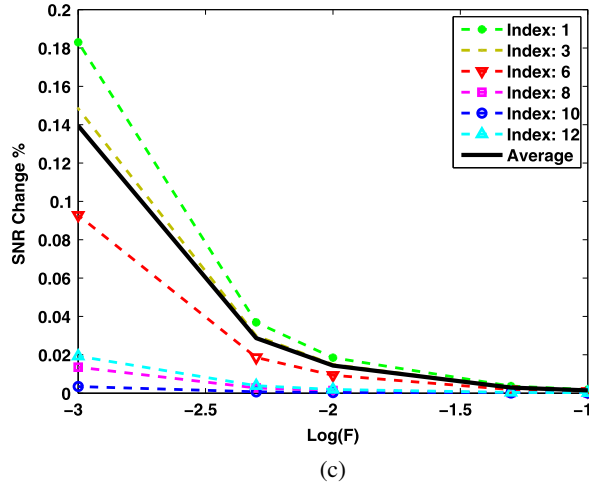
has the least SNR sensitivity for almost all intensity factors of the red channel; or in Figs. 7(b) and 8(b), for the green sensor, the greenish color patches (index = 1, 12) have lower SNR sensitivities compared with the other color samples. This conclusion is only true for dark current and read noise



(a)



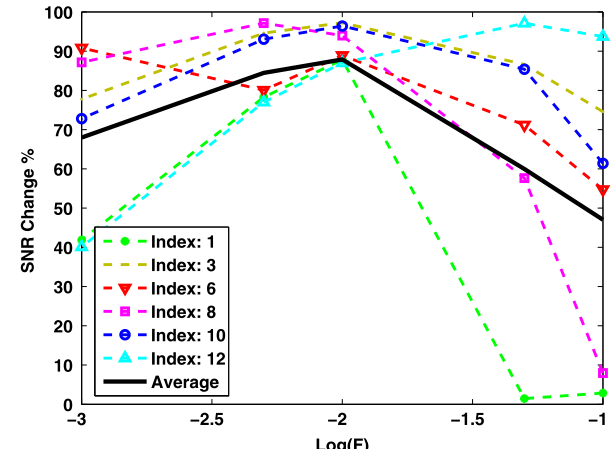
(b)



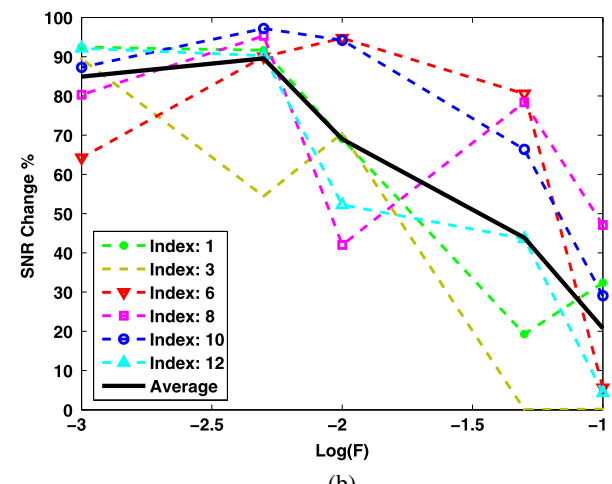
(c)

**Figure 8.** SNR sensitivity curves for the R, G, and B sensor types with respect to the read noise parameters for different color patches are plotted in (a), (b), and (c) respectively.

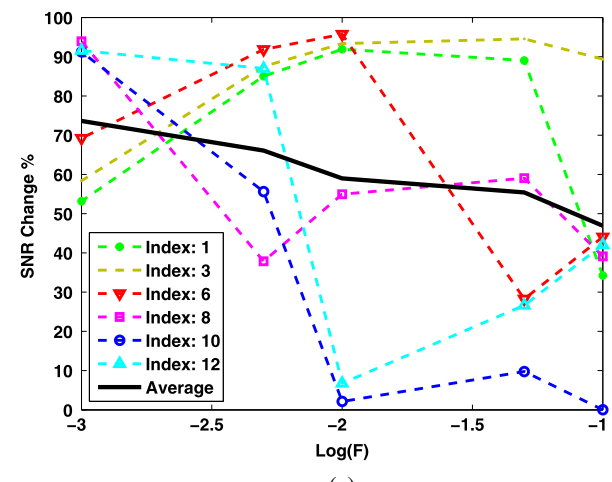
curves. Comparing the average SNR sensitivities of the three noise types reveals that read noise variations have the least impact on the SNR (less than 1%); then dark noise affects the SNR by between 1 and 9%; and the quantization noise has the most significant influence on the SNR.



(a)



(b)



(c)

**Figure 9.** SNR sensitivity curves for the R, G, and B sensor types with respect to the quantization noise for different color patches are plotted in (a), (b), and (c) respectively.

## CONCLUSION

In this work, we examined the effects of noise on color measurements of image sensors at low light levels. In this regard, a typical image sensor with a detailed noise model was implemented. The image sensor model was employed

in several experiments to investigate the quality of color measurements at low light intensities in the presence of noise.

The results can be summarized as follows: first, even an ideal image sensor without any device noise cannot measure consistent colors at very low light levels due to the photon noise; second, in contrast to the photon noise and read noise, which cause the generated samples at low light levels to be distributed around the high intensity samples, the dark current noise pushes the measurements towards the center of the chromaticity diagram (lower saturation values); third, for a single color patch, the distribution of noisy measured samples of an image sensor in low light situations forms an elliptical shape, and the size and inclination angle of the ellipse can give us some information about the type of noise affecting the measurements, and the color and luminance of the color patch; fourth, dark current induces a much more severe impact on color measurements in comparison to photon noise, read noise and quantization error; last but not least, the SNR sensitivity analysis showed that the presence of quantization noise does not cause a consistent change over the SNR value for different intensity factors, implying that this noise is little influenced by the light level change.

We believe that this work is relevant for many applications such as developing denoising algorithms, improving low light imaging, addressing low light image quality assessment techniques, and characterizing the noise of image sensors. Finally, this study could be further extended by incorporating the exposure time and ISO setting parameters into the model and then a set of optimal adjustments for the camera could be derived for different lighting conditions to obtain output images with the highest SNR values.

## REFERENCES

- <sup>1</sup> M. Rezagholizadeh and J. J. Clark, "Maximum entropy spectral modeling approach to mesopic tone mapping," *Proc. IS&T Twenty-first Color and Imaging Conf.* (IS&T, Springfield, VA, 2013), pp. 154–159.
- <sup>2</sup> M. P. Lucassen, P. Bijl, and J. Roelofsen, "The perception of static colored noise: detection and masking described by CIE94," *Color Res. Appl.* **33**, no. 3, 178–191 (2008).
- <sup>3</sup> D. Wueller, "Low light performance of digital still cameras," *SPIE 8667* (2013), p. 86671H.
- <sup>4</sup> A. Agah, A. Hassibi, J. D. Plummer, and P. B. Griffin, "Design requirements for integrated biosensor arrays," *Biomedical Optics 2005* (International Society for Optics and Photonics, 2005), pp. 403–413.
- <sup>5</sup> M. Nuutinen, O. Orenius, T. Saamanen, and P. Oittinen, "A reduced-reference method for characterizing color noise in natural images captured by digital cameras," *Proc. IS&T/SID Eighteenth Color and Imaging Conf.* (IS&T, Springfield, VA, 2010), pp. 80–85.
- <sup>6</sup> M. Rezagholizadeh and J. J. Clark, "Photon detection and color perception at low light levels," *11th Conference on Computer and Robot Vision (CRV)* (2014).
- <sup>7</sup> J. Pokorny, M. Lutze, D. Cao, and A. J. Zele, "The color of night: Surface color perception under dim illuminations," *Vis. Neurosci.* **23**, no. 3–4, 525–530 (2006).
- <sup>8</sup> J. J. McCann, "Colors in dim illumination and candlelight," *Proc. IS&T/SID Fifteenth Color and Imaging Conf.* (IS&T, Springfield, VA, 2007), pp. 313–318.
- <sup>9</sup> T. Ishida, "Color identification data obtained from photopic to mesopic illuminance levels," *Color Res. Appl.* **27**, no. 4, 252–259 (2002).
- <sup>10</sup> J. A. Ferwerda, S. N. Pattanaik, P. Shirley, and D. P. Greenberg, "A model of visual adaptation for realistic image synthesis," *Proc. 23rd Annual Conf. on Computer Graphics and Interactive Techniques* (ACM, 1996), pp. 249–258.
- <sup>11</sup> J. J. McCann and J. L. Benton, "Interaction of the long-wave cones and the rods to produce color sensations," *J. Opt. Soc. Am.* **59**, no. 1, 103–106 (1969).
- <sup>12</sup> J. Shin, N. Matsuki, H. Yaguchi, and S. Shioiri, "A color appearance model applicable in mesopic vision," *Opt. Rev.* **11**, no. 4, 272–278 (2004).
- <sup>13</sup> A. G. Kirk and J. F. O'Brien, "Perceptually based tone mapping for low-light conditions," *ACM Trans. Graph.* **30**, no. 4, 42 (2011).
- <sup>14</sup> J. Chen, K. Venkataraman, D. Bakin, B. Rodricks, R. Gravelle, P. Rao, and Y. Ni, "Digital camera imaging system simulation," *IEEE Trans. Electron Devices* **56**, no. 11, 2496–2505 (2009).
- <sup>15</sup> P. L. Vora, J. E. Farrell, J. D. Tietz, and D. H. Brainard, "Image capture: simulation of sensor responses from hyperspectral images," *IEEE Trans. Image Process.* **10**, no. 2, 307–316 (2001).
- <sup>16</sup> J. E. Farrell, P. B. Catrysse, and B. A. Wandell, "Digital camera simulation," *Appl. Opt.* **51**, no. 4, A80–A90 (2012).
- <sup>17</sup> J. E. Farrell, F. Xiao, P. B. Catrysse, and B. A. Wandell, "A simulation tool for evaluating digital camera image quality," *SPIE 5294* (2004), pp. 124–131.
- <sup>18</sup> S. W. Hasinoff, F. Durand, and W. T. Freeman, "Noise-optimal capture for high dynamic range photography," *2010 IEEE Conference on Computer Vision and Pattern Recognition (CVPR)* (IEEE, 2010), pp. 553–560.
- <sup>19</sup> M. Shohara and K. Kotani, "The dependence of visual noise perception on background color and luminance," *Picture Coding Symposium (PCS), 2010* (IEEE, 2010), pp. 594–597.
- <sup>20</sup> S.-J. Han, L. Xu, H. Yu, R. J. Wilson, R. L. White, N. Pourmand, and S. X. Wang, "CMOS integrated DNA microarray based on GMR sensors," *International Electron Devices Meeting 2006 (IEDM'06)* (IEEE, 2006), pp. 1–4.
- <sup>21</sup> R. W. Rodieck and R. W. Rodieck, *The First Steps in Seeing* (Sinauer Associates, Sunderland, 1998).
- <sup>22</sup> G. Wyszecki and W. S. Stiles, *Color Science* (Wiley, New York, 1982).
- <sup>23</sup> X. Liu, "CMOS image sensors dynamic range and SNR enhancement via statistical signal processing," Ph.D. dissertation (Stanford University, 2002).
- <sup>24</sup> K. Sperlich and H. Stolz, "Quantum efficiency measurements of (EM) CCD cameras: high spectral resolution and temperature dependence," *Meas. Sci. Technol.* **25**, no. 1, 015502 (2014).
- <sup>25</sup> K. K. Hamamatsu, *Opto-semiconductor Handbook* (Hamamatsu Photonics, Japan, 2009).
- <sup>26</sup> K. Barnard, L. Martin, B. Funt, and A. Coath, "A data set for color research," *Color Res. Appl.* **27**, no. 3, 147–151 (2002).
- <sup>27</sup> CIE191:2010, "Recommended system for mesopic photometry based on visual performance," *Color Res. Appl.* **36**, no. 1, 46–125 (2011) [Online]. Available: <http://dx.doi.org/10.1002/col.20669>.
- <sup>28</sup> K. Barnard and B. Funt, "Camera characterization for color research," *Color Res. Appl.* **27**, no. 3, 152–163 (2002).
- <sup>29</sup> L. I. Smith, (2002) A tutorial on principal components analysis.
- <sup>30</sup> C. Stark, "DSLR vs. CCD: A bench test comparison," *AstroPhoto Insight Magazine (Special Hardware Issue)* **3**, no. 7, 32–41 (2007) [Online]. Available: [http://www.stark-labs.com/craig/resources/Articles-&Reviews/DSLRvsCCD\\_API.pdf](http://www.stark-labs.com/craig/resources/Articles-&Reviews/DSLRvsCCD_API.pdf).